Steady-State Angle Stability Analysis of Parallel Grid-Forming Converters in Current Saturation Mode

Yonghui Liu, *Member, IEEE*, Yue Wang, *Member, IEEE*, Xiaokang Liu, *Senior Member, IEEE*, Minghao Wang, *Member, IEEE*, Z h a o X u , *Senior Member, IEEE*, and Hang Liu

***Abstract*—Grid-forming converters (GFCs) usually operate in parallel to supply power to unknown loads. Nevertheless, unknown loads may lead to overcurrent, causing parallel GFCs to enter the current saturation mode (CSM). The steady-state angle stability of parallel GFCs in CSM is crucial for ensuring reliable operation under unknown loads, yet this issue has not been studied previously. This article presents a novel power model for parallel GFCs in CSM and conducts the first-ever investigation of steady-state angle stability in this context. The analysis results reveal that the steady-state angle stability of the equilibrium points (EPs) under overall inductive load is opposite to that under overall capacitive load. Specifically, it is shown that the EP with even power allocation is unstable, and the parallel GFCs will transition to the EP with circulating currents in the presence of overall capacitive loads. Eventually, all the capacity of GFCs is occupied by the circulating currents, failing to supply voltage to the loads. The proposed model and analysis are validated through experimental results, highlighting the significant risk of power supply failure for parallel GFCs in CSM and providing general guidance for the operation of GFCs in parallel.**

***Index Terms*—Current saturation mode (CSM), grid-forming converters (GFCs), parallel connection, steady-state stability.**

I. Introduction

GRID-FORMING converters (GFCs) are key components in future power-electronic-based power systems. They typically operate in voltage-control mode (VCM). However, under conditions of overload or low voltage, GFCs will transition to current-saturation mode (CSM) by limiting the reference of the inner current loop [1]. While the stability of GFCs in VCM has been well studied [2], [3], the stability of GFCs in CSM is just gaining attention in recent years.

Previous studies have examined the transient stability of a GFC in CSM under grid voltage sags [4], [5], [6]. These studies have considered the GFC as a single unit tied to an infinite bus. However, GFCs are typically utilized in systems with high penetration of power electronic converters, which are essentially parallel-GFC systems rather than infinite buses. Parallel GFCs usually function as the interface of renewable energy sources or storage batteries to supply power to areas with unknown loads and are prone to entering CSM due to source power deficiency or overload. In some industrial applications, parallel GFCs have been observed to gradually lose phase synchronization after entering CSM. Nevertheless, to the best of the authors' knowledge, the underlying mechanism of this phenomenon remains unexplored.

To fill this gap, this article conducts the first-ever investigation of the steady-state angle stability of parallel GFCs in CSM. The analysis results indicate that the state of synchronized phases among parallel GFCs in CSM is stable under inductive loads but unstable under capacitive loads, shedding light on the previously observed phenomenon.

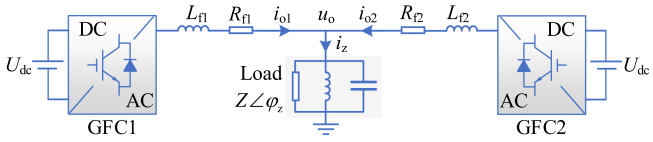

Fig. 1. Illustration of the studied system with parallel GFCs and loads.

II. System Modeling

Without loss of generality, the modeling and analysis are performed on a sample system with two GFCs, as shown in Fig. 1. All the variables are described by their per-unit values hereinafter. Z and φ_z are the total amplitude and phase of arbitrary loads. u_o is the point of common coupling (PCC) voltage. i_z is the load current, which is the sum of the output currents of

This work was supported in part by the Natural Science Foundation of China under Grant 51777159 and in part by the HK PolyU Research Institute for Smart Energy under strategic supporting Scheme P0039642. *(Corresponding authors: Yue Wang; Xiaokang Liu.)*

Yonghui Liu is with the School of Electrical Engineering, Xi'an Jiaotong University, Xi'an 710049, China, and also with the Department of Electrical Engineering, The Hong Kong Polytechnic University, 100872, Hong Kong (e-mail: liuyonghui@stu.xjtu.edu.cn).

Yue Wang is with the School of Electrical Engineering, Xi'an Jiaotong University, Xi'an 710049, China (e-mail: davidwangyue@mail.xjtu.edu.cn).

Xiaokang Liu is with the Department of Electronics, Information and Bioengineering, Politecnico di Milano 20133 Milano, Italy (e-mail: xiaokang.liu@polimi.it).

Minghao Wang and Zhao Xu are with the Department of Electrical Engineering, The Hong Kong Polytechnic University, 100872, Hong Kong (e-mail: mhwang@polyu.edu.hk; eezhaoxu@polyu.edu.hk).

Hang Liu is with the State Grid Zhengzhou Electric Power Supply Company, Zhengzhou 450000, China (e-mail: lhxjtu2019@stu.xjtu.edu.cn).

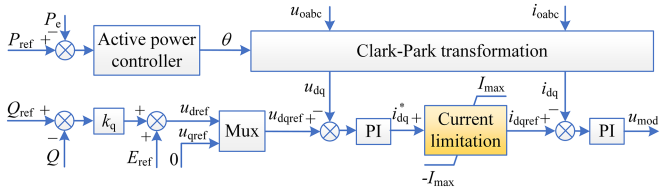

Fig. 2. Control framework of a GFC.

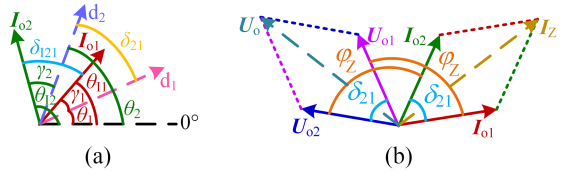

Fig. 3. Vector diagrams. (a) Currents and *d*-axes. (b) Currents and voltages.

the two GFCs, i_{o1} and i_{o2}. L_f and R_f are the filter inductance and resistance.

The framework of a GFC controller is illustrated in Fig. 2. The active power controller is considered to satisfy

$$2H_i\frac{d\omega_i}{dt} = P_{refi} - P_{ei} - D_i(\omega_i - 1) \tag{1}$$

$$\frac{d\theta_i}{dt} = \omega_i \tag{2}$$

where the subscript *i* represents the series number of the GFC. *H* is the inertia time constant, and *D* is the per-unit damping factor. ω is the per-unit real-time angular frequency. P_e and P_{ref} are the per-unit output active power and its reference, respectively. θ is the phase of the *d*-axis of the GFC.

The amplitude of the current reference is limited to I_{max} in CSM. The specific current-limiting method does not influence the analysis results, as demonstrated by the following analysis. It is assumed that the GFCs use the identical base value to calculate the per-unit value and that $i_{odq} = i_{dqref}$.

A. Power Calculation

The vector diagrams of two GFCs in CSM are depicted in Fig. 3.

In Fig. 3(a), d_1 and d_2 are the *d*-axes of GFC1 and GFC2, respectively. The current phases of GFC1 and GFC2, θ_{I1} and θ_{I2}, satisfy

$$\begin{cases}\theta_{I1} = \theta_1 + \gamma_1\\ \theta_{I2} = \theta_2 + \gamma_2\end{cases} \tag{3}$$

where θ_1 and θ_2 are the phases of the d-axes of GFC1 and GFC2, respectively. γ_1 and γ_2 are the phases of currents with reference to the pertinent *d*-axis of GFC1 and GFC2.

The phase difference between the d-axes of GFC1 and GFC2 is defined as

$$\delta_{21} = \theta_2 - \theta_1, \tag{4}$$

The phase difference between $\boldsymbol{I}_{o1}$ and $\boldsymbol{I}_{o2}$, defined as δ_{I21}, can be calculated as

$$\delta_{I21} = \theta_{I2} - \theta_{I1} = \delta_{21} + \gamma_2 - \gamma_1. \tag{5}$$

As shown in Fig. 3(b), the load current vector $\boldsymbol{I}_z$ is synthesized by the output current vectors of GFC1 and GFC2, $\boldsymbol{I}_{o1}$ and $\boldsymbol{I}_{o2}$. By defining the voltage drops on the load, contributed by $\boldsymbol{I}_{o1}$ and $\boldsymbol{I}_{o2}$, as $\boldsymbol{U}_{o1}$ and $\boldsymbol{U}_{o2}$, respectively, i.e.,

$$\begin{cases}\boldsymbol{U}_{o1} = \boldsymbol{I}_{o1}Z\\ \boldsymbol{U}_{o2} = \boldsymbol{I}_{o2}Z\end{cases}, \tag{6}$$

the PCC voltage vector $\boldsymbol{U}_o$ can be divided into $\boldsymbol{U}_{o1}$ and $\boldsymbol{U}_{o2}$. The active power of GFC1 and GFC2 is then calculated as

$$\begin{cases}P_{e1} = U_{o1}I_{o1}\cos\varphi_z + U_{o2}I_{o1}\cos(\varphi_z + \delta_{I21})\\ P_{e2} = U_{o2}I_{o2}\cos\varphi_z + U_{o1}I_{o2}\cos(\varphi_z - \delta_{I21})\end{cases}. \tag{7}$$

By substituting (6) into (7), and considering $I_{o1} = I_{o2} = I_{max}$ in CSM, the corresponding power model in CSM is proposed as

$$\begin{cases}P_{e1} = I_{max}^2 Z[\cos\varphi_z + \cos(\varphi_z + \delta_{I21})]\\ P_{e2} = I_{max}^2 Z[\cos\varphi_z + \cos(\varphi_z - \delta_{I21})]\end{cases}. \tag{8}$$

B. State-Space Equation and Equilibrium Point

Substituting (8) into (1) gives

$$\frac{d\omega_1}{dt} = \frac{-D_1(\omega_1 - 1) + P_{ref1} - I_{max}^2 Z[\cos\varphi_z + \cos(\varphi_z + \delta_{I21})]}{2H_1} \tag{9}$$

$$\frac{d\omega_2}{dt} = \frac{-D_2(\omega_2 - 1) + P_{ref2} - I_{max}^2 Z[\cos\varphi_z + \cos(\varphi_z - \delta_{I21})]}{2H_2}. \tag{10}$$

If $H_1 = H_2 = H$, $D_1 = D_2 = D$, and $P_{ref1} = P_{ref2} = P_{ref}$, by denoting $\omega_{21} = \omega_2 - \omega_1$ and subtracting (9) from (10), the differential equation of ω_{21} is derived as

$$\frac{d\omega_{21}}{dt} = \frac{-D\omega_{21} - 2I_{max}^2 Z\sin\varphi_z\sin\delta_{I21}}{2H}. \tag{11}$$

Meanwhile, by combining (2) and (4), it can be derived that

$$\frac{d\delta_{21}}{dt} = \omega_{21}. \tag{12}$$

According to (5), (11), and (12), the frequency difference $\bar{\omega}_{21}$ and phase difference $\bar{\delta}_{I21}$ of the equilibrium points (EPs) in each period satisfy

$$(\bar{\omega}_{21}, \bar{\delta}_{I21}) = (0, k\pi), k \in \mathbb{Z}. \tag{13}$$

III. Steady-State Angle Stability Analysis

A. Steady-State Angle Stability Condition

The linearized state-space function can be deduced from (5), (11), and (12) as

$$\begin{bmatrix}\dot{\omega}_{21} & \dot{\delta}_{21}\end{bmatrix}^T = \mathbf{A}\begin{bmatrix}\Delta\omega_{21} & \Delta\delta_{21}\end{bmatrix}^T \tag{14}$$

where $\mathbf{A}$ is the Jacobian matrix evaluated at the EPs, which can be derived as

$$\mathbf{A}=\begin{bmatrix} \frac{-D}{2H} & -\frac{I_{\max}^2 Z}{H}\sin\varphi_z\cos\bar{\delta}_{I21}\left[1+\frac{\partial(\gamma_2-\gamma_1)}{\partial\delta_{21}}\right] \\ 1 & 0 \end{bmatrix} \quad (15)$$

where $\partial(\gamma_2-\gamma_1)/\partial\delta_{21}$ is the partial derivative of $(\gamma_2-\gamma_1)$ w.r.t. δ_{21}.

According to the nonlinear theory [7], as long as the real parts of all the eigenvalues of $\mathbf{A}$ are negative, the EP is a stable equilibrium point (SEP). Otherwise, the EP is an unstable equilibrium point (UEP). According to (15), the eigenvalues of $\mathbf{A}$ can be calculated as

$$\lambda_{1,2}=\frac{-D}{4H}\pm\frac{1}{2}\sqrt{\left(\frac{D}{2H}\right)^2-4\frac{I_{\max}^2 Z}{H}\sin\varphi_z\cos\bar{\delta}_{I21}\left[1+\frac{\partial(\gamma_2-\gamma_1)}{\partial\delta_{21}}\right]}. \quad (16)$$

By considering that D and H are positive and enforcing negative real parts of $\lambda_{1,2}$, the steady-state stable condition can be derived as

$$\sin\varphi_z\cos\bar{\delta}_{I21}\left[1+\partial(\gamma_2-\gamma_1)/\partial\delta_{21}\right]>0. \quad (17)$$

If $\partial(\gamma_2-\gamma_1)/\partial\delta_{21}>-1$, (17) will be equivalent to

$$\sin\varphi_z\cos\bar{\delta}_{I21}>0. \quad (18)$$

Conversely, if $\partial(\gamma_2-\gamma_1)/\partial\delta_{21}<-1$, (17) will be equivalent to

$$\sin\varphi_z\cos\bar{\delta}_{I21}<0. \quad (19)$$

A significant principle is revealed by (17)–(19), i.e., the overall load property influences the steady-state stability of EPs. Whether (18) or (19) is valid, the steady-state angle stability of any EP under overall inductive load is opposite to that under overall capacitive load.

It is noted that $\partial(\gamma_2-\gamma_1)/\partial\delta_{21}$ denotes the effect of the current-limiting control (including current limitation and voltage loop anti-windup control) on the steady-state angle stability. If $\partial(\gamma_2-\gamma_1)/\partial\delta_{21}=0$, the steady-state angle stability condition is determined by the power loop without the influence of current-limiting control, and (18) holds for that case. The contrast between (18) and (19) indicates that the current-limiting control will reverse the effect of the power loop once $\partial(\gamma_2-\gamma_1)/\partial\delta_{21}<-1$. Here, the power loop is the outermost loop, whereas the current-limiting control is an inner loop. If the inner loop reverses the impact of the outermost loop on the steady-state stability, it indicates a design flaw in the current-limiting control that prevents the inner loop from achieving the goal of the outermost power loop. This scenario is unacceptable for practical applications. Hence, it is considered that $\partial(\gamma_2-\gamma_1)/\partial\delta_{21}>-1$ for a reasonable current-limiting control, and the pertinent stable condition is given by (18).

B. Steady-State Angle Stability Analysis

The SEPs and UEPs under inductive load ($0°<\varphi_z\le 90°$) are denoted as L-SEPs and L-UEPs, respectively. According to (13) and (18), δ_{I21} of L-SEPs and L-UEPs satisfy

$$\begin{cases}\bar{\delta}_{I21}=2m\pi, m\in\mathbb{Z}, \text{for L}-\text{SEPs}\\ \bar{\delta}_{I21}=(2m+1)\pi, m\in\mathbb{Z}, \text{for L}-\text{UEPs}\end{cases}. \quad (20)$$

By denoting the SEPs and UEPs under capacitive load ($-90°\le\varphi_z<0°$) as C-SEPs and C-UEPs, δ_{I21} of C-SEPs and C-UEPs satisfy

$$\begin{cases}\bar{\delta}_{I21}=(2m+1)\pi, m\in\mathbb{Z}, \text{for C}-\text{SEPs}\\ \bar{\delta}_{I21}=2m\pi, m\in\mathbb{Z}, \text{for C}-\text{UEPs}\end{cases}. \quad (21)$$

Based on (8), (20), and (21), the power-angle curves of GFC1 and GFC2 can be plotted in Fig. 4. As shown in Fig. 4(a), under overall inductive loads, it holds that $\delta_{I21}=0$ and $P_{e1}=P_{e2}=2I_{\max}^2 Z\cos\varphi_z$ at L-SEP, indicating that all currents flow into loads without circulating between GFCs. Nevertheless, under overall capacitive loads, as illustrated in Fig. 4(b), $\delta_{I21}=\pm\pi$ and $P_{e1}=P_{e2}=0$ at C-SEPs, indicating that all currents will eventually circulate between GFCs without flowing into loads.

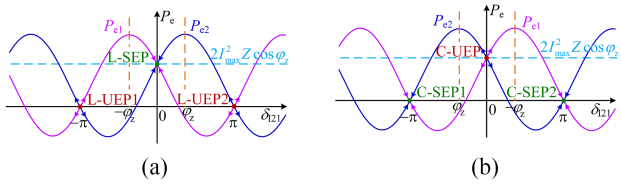

(a) (b)

Fig. 4. Power-angle curves of GFC1 and GFC2. (a) With overall inductive loads ($0°<\varphi_z\le 90°$). (b) With overall capacitive loads ($-90°\le\varphi_z<0°$).

The above analysis indicates that the parallel GFCs in CSM can maintain stability under overall inductive loads at the L-SEP with even power allocation, but cannot operate under overall capacitive loads without circulating currents. Once the parallel GFCs operate in CSM and the loads are overall capacitive, the GFCs will fail to supply power to loads.

C. Discussion on Analysis Generality

For a multiple-GFC-parallel system, the modeling and analysis can be conducted using the same approach proposed in this article. As long as H, D, P_{ref}, and $I_{\max}$ of those GFCs are identical, respectively, the stable condition will be the same as (18).

When H, D, P_{ref}, and $I_{\max}$ of GFCs differ, the power modeling approach proposed in this paper remains applicable. But the existence of the EPs needs to be checked before the stability analysis according to the state-space equation similar to (9)–(12). If EPs exist, the stable condition will have a complex expression due to parameter distinctions. Future research needs to focus on how to ensure the existence of EPs and simplify the stable condition under these conditions.

In practice, it is common for GFCs manufactured by the same company to have identical H, D, P_{ref}, and $I_{\max}$. These converters are usually connected in parallel as the interfaces for renewable energy sources or storage batteries to unknown loads. However, the deficiency of renewable energy sources, the withdrawal of other power supplies, or the short circuit of some loads may cause these converters to enter CSM frequently. The findings

TABLE I
MAIN PARAMETERS

Description	Symbol	Value of GFC
Rated DC-link voltage of GFC	U_{dc}	900 V
Rated line voltage of GFC	U_{ab}	480 Vrms
Rated power	S_n	30 kW
Rated angular frequency	ω_s	314.16 rad/s
Filter inductance	L_{f1}, L_{f2}	2 mF
Filter resistance	R_{f1}, R_{f2}	1 mΩ
Current limitation magnitude	I_{max}	56 A (1.1 p.u.)
Inertia time constant	H	0.26 s
Damping factor	D	251 p.u.
Active power reference	P_{ref}	0 p.u.
Proportional coefficient of voltage controller	k_{vp}	0.5
Integral coefficient of voltage controller	k_{vi}	20
Proportional coefficient of current controller	k_{cp}	5
Integral coefficient of current controller	k_{ci}	500

presented in this article highlight a significant risk of power supply failure for these actual applications.

IV. EXPERIMENTAL VERIFICATION

To validate the theoretical findings, hardware-in-the-loop experiments that mirror the system depicted in Fig. 1 are conducted. The two GFCs in the experiment adopt identical grid-forming controllers, as shown in Fig. 2. Both GFCs were configured with the same parameters, which are itemized in Table I.

The initial state of the experiment involves overall loads of 50 Ω (6.5 p.u.) and the GFCs operating in VCM with even power allocation.

A. Verification With Identical GFC Current-Limiting Method

To test the case where GFCs adopt the identical current-limiting method, the *d*-axis prioritized current-limiting method [8] is adopted in both GFCs. Under this method, the limited current references satisfy

$$\begin{cases} i_{dref} = i_d^*/|i_d^*| \cdot \min\left(|i_d^*|, I_{max}\right) \\ i_{qref} = i_q^*/|i_q^*| \cdot \min\left(|i_q^*|, \sqrt{(I_{max})^2 - (i_{dref})^2}\right) \end{cases}. \quad (22)$$

To test the case of the overall inductive load, a 6.1 mH (0.25 p.u.) inductor in series with a 1 Ω (0.13 p.u.) resistor is connected at t_1. As shown in Fig. 5(a), the amplitudes of the currents i_{a1} and i_{a2} increase to approximately 56 A (1.1 p.u.) at t_1, indicating that the GFCs are switched into CSM after t_1 due to overloading. During CSM, the current phase difference between the two GFCs, δ_{I21}, is kept at zero, indicating that the two GFCs send identical active power larger than P_{ref} to the loads without circulating current. Consequently, as shown in Fig. 5(b), the frequencies of both GFCs, f_1 and f_2, are equal and below 50 Hz. The PCC voltage u_a remains stable during CSM. The state after t_1 in Fig. 5 corresponds to the L-SEP in Fig. 4(a), which satisfies (18). The results demonstrate that parallel GFCs with an identical current-limiting method can stably operate with even power allocation under inductive loads.

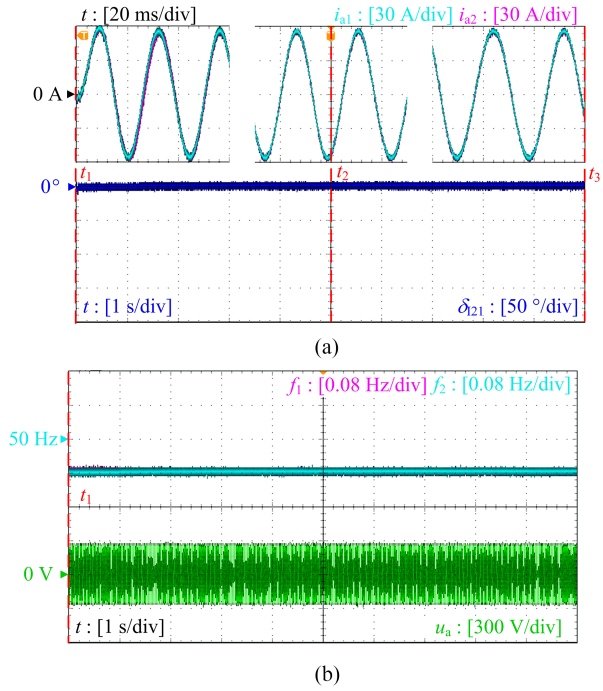

Fig. 5. Waveforms under overall inductive load and with an identical current-limiting method. (a) Phase-A currents of GFCs and current phase difference between GFC2 and GFC1. (b) Frequencies of GFCs and PCC voltage (phase A).

For the case of the overall capacitive load, a 0.83 mF capacitor (whose per-unit reactance is 0.5 p.u.) in series with a 1 Ω (0.13 p.u.) resistor is connected to PCC at t_1. The currents of the GFCs and their phase difference are shown in Fig. 6(a). After t_1, the current amplitudes increase to approximately 56 A, and the GFCs enter CSM. The current of GFC2 increasingly leads that of GFC1 from 0° to 180°. Eventually, all the output currents of GFCs are circulating currents between themselves. Correspondingly, the PCC voltage magnitude declines to zero [see Fig. 6(b)]. After dynamic adjustment, the frequencies of GFCs eventually stabilize at 50 Hz, indicating that their active power equals P_{ref} of 0 p.u.

At t_1, the operating state (see Fig. 6) corresponds to C-UEP in Fig. 4(b), satisfying (19) but not (18). The experimental results in Fig. 6 manifest that the system cannot stabilize at that state. Thereby, the results agree with the consideration of $\partial(\gamma_2-\gamma_1)/\partial\delta_{21} > -1$ for simplifying (17). The state at the end of Fig. 6 corresponds to C-SEP2 in Fig. 4(b), satisfying (18). The results in Fig. 6 indicate that the GFCs with the identical current-limiting method deviate from the state of phase synchronization and ultimately end up with all current circulating between GFCs when the load is overall capacitive.

B. Verification With Different GFC Current-Limiting Methods

To verify the applicability of the theoretical findings to different current-limiting methods, the *d*-axis current prioritization and the current vector angle prioritization approaches are adopted for GFC1 and GFC2, respectively.

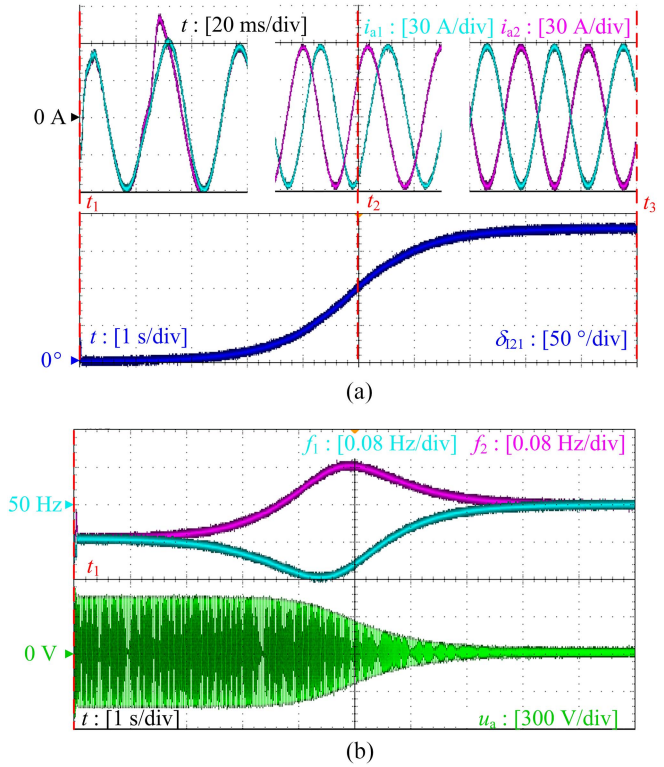

Fig. 6. Waveforms under overall capacitive load and with an identical current-limiting method. (a) Phase-A currents of GFCs and current phase difference between GFC2 and GFC1. (b) Frequencies of GFCs and PCC voltage (phase A).

Under the current vector angle prioritized current-limiting method, the limited current references satisfy

$$\begin{cases} i_{\text{dref}} = i_{\text{d}}^*/|i_{\text{d}}^*| \cdot \min\left(|i_{\text{d}}^*|, I_{\max}|i_{\text{d}}^*| \Big/ \sqrt{(i_{\text{d}}^*)^2 + (i_{\text{q}}^*)^2}\right) \\ i_{\text{qref}} = i_{\text{q}}^*/|i_{\text{q}}^*| \cdot \min\left(|i_{\text{q}}^*|, I_{\max}|i_{\text{q}}^*| \Big/ \sqrt{(i_{\text{d}}^*)^2 + (i_{\text{q}}^*)^2}\right) \end{cases}. \tag{23}$$

Results similar to the previous cases with inductive and capacitive loads are obtained, as shown in Figs. 7 and 8, respectively. Though the distinct current-limiting methods lead to different dynamic trajectories of variables from those in Figs. 5 and 6, the steady-state results for both systems are the same. When the load is inductive, the parallel GFCs in CSM can be stabilized with even power allocation. Conversely, for a capacitive load, the parallel GFCs gradually transition from the state of even power allocation to the state dominated by the circulating current. Eventually, they lose phase synchronization and fail to supply power to the load.

The experimental results have verified the correctness of the theoretical analysis and its applicability to the parallel GFCs under different industrial current-limiting methods. Though not reported here for brevity, the results for the multiple-GFC-parallel system are similar to those of the two-GFC-parallel system.

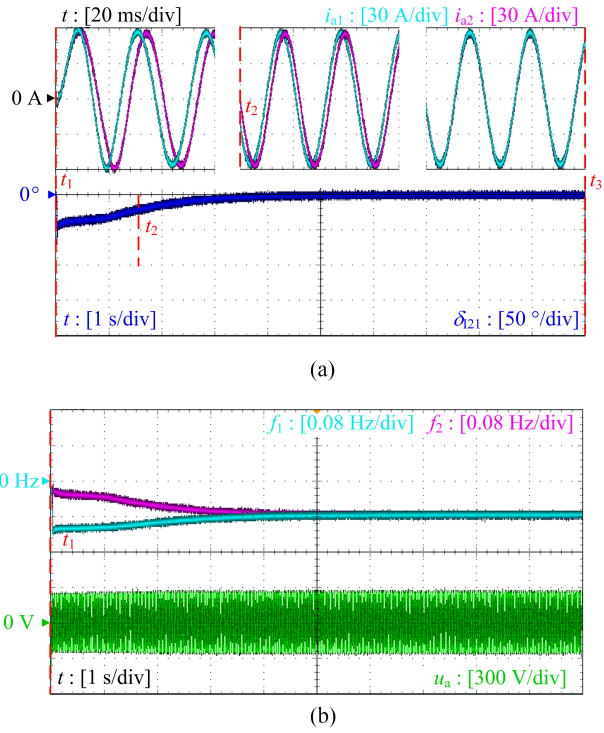

Fig. 7. Waveforms under overall inductive load and with different current-limiting methods. (a) Phase-A currents of GFCs and current phase difference between GFC2 and GFC1. (b) Frequencies of GFCs and PCC voltage (phase A).

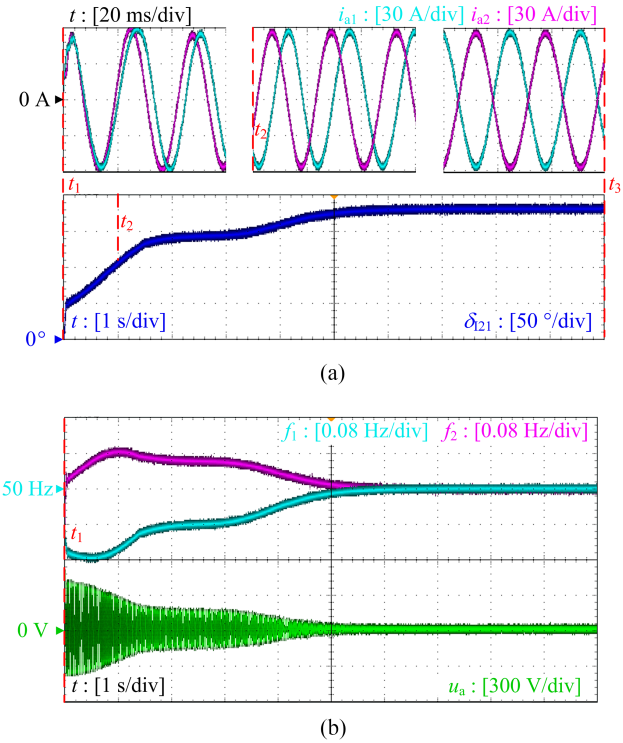

Fig. 8. Waveforms under overall capacitive load and with different current-limiting methods. (a) Phase-A currents of GFCs and current phase difference between GFC2 and GFC1. (b) Frequencies of GFCs and PCC voltage (phase A).

V. Conclusion

To investigate the steady-state angle stability of the parallel GFCs in CSM, a power model for the parallel GFCs in CSM is first proposed in this article. Based on the model, the state-space equation is derived, and the two EPs under identical control parameters in each period are calculated. The steady-state angle stability in the vicinity of the EPs is analyzed according to the Jacobian matrix. It is found that for the inductive load, the EPs where power is evenly allocated between GFCs are stable, while the EPs with circulating current between GFCs are unstable. Once GFCs operate in CSM under overall capacitive load, the EPs with even power allocation between GFCs are unstable, while the EPs with all the current circulating between GFCs are stable. The experimental results verify the correctness of the theoretical analysis under different current-limiting methods.

The conclusions are generally applicable to multiple-GFC-parallel systems as long as the GFCs have identical active power controller parameters and current amplitude limitations. The findings serve as an important reminder for industrial applications that parallel GFCs operating in CSM will lose phase synchronization and fail to supply power to capacitive loads. Moreover, the work motivates further research on potential solutions to address this issue.

References

[1] B. Fan and X. Wang, "Equivalent circuit model of grid-forming converters with circular current limiter for transient stability analysis," *IEEE Trans. Power Syst.*, vol. 37, no. 4, pp. 3141–3144, Jul. 2022.

[2] T. Liu and X. Wang, "Transient stability of single-loop voltage-magnitude controlled grid-forming converters," *IEEE Trans. Power Electron.*, vol. 36, no. 6, pp. 6158–6162, Jun. 2021.

[3] L. Xiong, X. Liu, Y. Liu, and F. Zhuo, "Modeling and stability issues of voltage-source converter dominated power systems: A review," *CSEE J. Power Energy Syst.*, vol. 8, no. 6, pp. 1530–1549, 2022.

[4] B. Fan and X. Wang, "Fault recovery analysis of grid-forming inverters with priority-based current limiters," *IEEE Trans. Power Syst.*, early access, Nov. 10, 2022, doi: 10.1109/TPWRS.2022.3221209.

[5] K. G. Saffar, S. Driss, and F. B. Ajaei, "Impacts of current limiting on the transient stability of the virtual synchronous generator," *IEEE Trans. Power Electron.,* vol. 38, no. 2, pp. 1509–1521, Feb. 2023.

[6] L. Huang, H. Xin, Z. Wang, L. Zhang, K. Wu, and J. Hu, "Transient stability analysis and control design of droop-controlled voltage source converters considering current limitation," *IEEE Trans. Smart Grid*, vol. 10, no. 1, pp. 578–591, Jan. 2019.

[7] H. K. Khalil, *Nonlinear Systems*. Englewood Cliffs, NJ, USA: Prentice-Hall, 2002.

[8] Z. Shuai, *Transient Characteristics, Modelling and Stability Analysis of Microgrid*. Berlin, Germany: Springer, 2021.